Nano-scale thin film investigations with slow polarized muons

2004 J. Phys.: Condens. Matter 16 S4583

(http://iopscience.iop.org/0953-8984/16/40/010)

INSTITUTE OF PHYSICS PUBLISHING JOURNAL OF PHYSICS: CONDENSED MATTER

J. Phys.: Condens. Matter **16** (2004) S4583–S4601 PII: S0953-8984(04)84693-9

Nano-scale thin film investigations with slow polarized muons

E Morenzoni[1], T Prokscha[1], A Suter[1], H Luetkens[1,2] and R Khasanov[1,3]

[1] Paul Scherrer Institut, Laboratory for Muon Spin Spectroscopy, CH-5232 Villigen PSI, Switzerland
[2] Institut für Metallphysik und Nukleare Festkörperphysik, TU Braunschweig, D-38106 Braunschweig, Germany
[3] Physik-Institut der Universität Zürich, CH-8057 Zürich, Switzerland

E-mail: elvezio.morenzoni@psi.ch

Received 8 April 2004
Published 24 September 2004
Online at stacks.iop.org/JPhysCM/16/S4583
doi:10.1088/0953-8984/16/40/010

Abstract

Muons with 100% spin polarization and whose energy can be continuously varied from 0.5 to 30 keV provide a novel extension of the μSR technique allowing depth dependent studies of thin films and multilayered structures in the range from ∼1 to ∼200 nm. For example it is possible to study magnetic field profiles near the surface of superconductors and directly determine fundamental quantities such as the magnetic penetration depth. Low energy muons (LE-μ^+) also allow mapping the spin polarization in multilayered structures, for instance that of the conduction electrons of a non-magnetic buried layer in between thin ferromagnetic layers.

(Some figures in this article are in colour only in the electronic version)

1. Introduction

The study of the magnetic and electronic properties of thin films has become in recent years one of the most active areas of research. This development is motivated scientifically as well as by the need and expectation for increasingly smaller and more efficient devices for technological applications. Of special interest are structures with nanometre dimensions. Reducing one or more dimensions of a physical system down to the nanometre scale can provide new insight into fundamental physical mechanisms. The surface and near surface regions of bulk material behave differently due to the loss of periodicity in one dimension and the disturbance caused by terminating the solid in a surface. At interfaces the proximity to other layers leads to novel interesting phenomena of interplay and coexistence of different ground states. A detailed knowledge of the magnetic and electronic characteristics of nanomaterials is also a prerequisite

to tailoring their functions in a controlled way and requires experimental techniques capable of probing them on the nanometre length scale.

Spin polarized muons have long been used to study magnetic and electronic properties of matter. The μSR results have added significantly to our knowledge and understanding of the complex phenomenology of the superconducting and magnetic state as well as in other domains of physics (e.g. semiconductors) and chemistry (e.g. radical chemistry, organic materials) [1]. So far, the major drawback of the technique has been its limitation to bulk studies of matter. However, μSR as a nuclear solid state technique and the positive muons as a local probe with specific, unique properties can also meet the challenge of studies on the nanometre scale. Essentially all the advantages offered by the polarized positive muons and the various μSR techniques (local highly sensitive magnetic and spin probe, proton/hydrogen isotope, time window complementing neutron scattering and NMR or macroscopic methods, possibility to perform experiments in zero magnetic field with no principal restriction to which materials can be implanted) can be used to study thin films, near surface regions, multilayers and superlattices composed of high temperature superconductors, magnetic materials, dielectrics, etc, making the muon a novel tool and μSR play its role as an advanced sensitive analytical technique.

The bulk sensitivity is a consequence of the energy scale of the pion decay from which the muons originate with a kinetic energy of $\sim$4.1 MeV. For thin film studies spin-polarized muon beams with tunable energies from a few eV to several keV and narrow energy distribution are required. Recently a beam with such characteristics has been developed at the Paul Scherrer Institute and first experiments have been performed. Its unique characteristics lie in the combination of μSR capability and depth sensitivity on the nm scale (LE-μSR). In this paper we review the state of the art of this novel μSR technique and give some representative examples of investigations.

2. Polarized muons for low-energy μSR spectroscopy

The conventionally used 'surface' muons with an initial implantation energy of about 4 MeV have stopping ranges in a solid varying from 0.1 to $\sim$1 mm with a wide distribution of about 20% of the mean value. Ideally, to extend the μSR technique to thin film studies or to obtain depth selective information one would like to have available a source of muons with just a few eV energy and then re-accelerate them to the desired energy.

By controlling their kinetic energy muons can be implanted at well-defined depths ranging from a few nanometres to a few hundred nanometres (see figure 1). Since the 1980s several methods have been proposed to slow down muons with initially MeV energies. Conventional cooling methods to reduce momentum and momentum spread, such as electron or stochastic cooling, are too slow for muons, where rapid action is required within a few μs. Phase-space compression of an energetic beam by deceleration and transport in pulsed electric and magnetic field or ionization cooling by one-directional acceleration under transverse and longitudinal slowing-down [2, 3] have proven too cumbersome for practical applications. A very simple way to slow down charged particles is to thermalize them partially or totally in matter. Slow beams of positrons and positronium are obtained for instance by bombarding solid foils with energetic particles. In some well selected materials, the interaction of charged particles with the solid constituents leads to a preferential emission probability at energies in the sub-eV or eV range. Based on an analogous principle two lines of developments have been actively pursued for muons:

(i) laser resonant ionization of thermal muonium (Mu) in vacuum produced from a hot metal surface, and

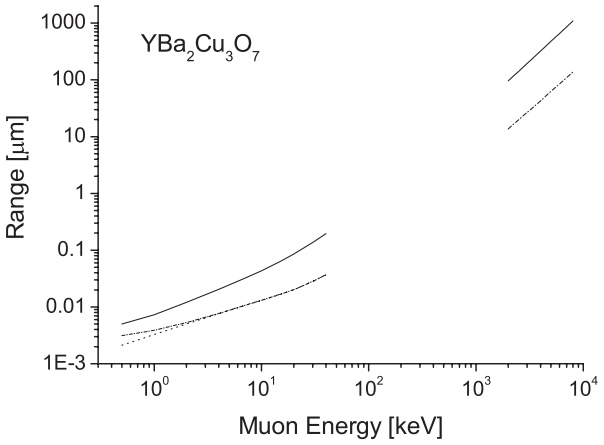

Figure 1. Mean (straight curve) and rms (dash–dotted curve) projected range of positive muons implanted in $YBa_2Cu_3O_{7-\delta}$ as a function of kinetic energy. An absolute energy uncertainty of 400 eV for low energy muons and a relative uncertainty of 6% for the energetic ones has been assumed. The dotted curve at low energies displays the intrinsic resolution for a monoenergetic beam.

(ii) moderation of surface muons in wide band gap insulators, particularly van der Waals bound solids.

The first method needs a pulsed muon beam synchronized to a laser system. Demonstration of this principle has been achieved [4]. However, at the moment the slow muon intensity reached is too low to allow the routine utilization of these particles as magnetic microprobes. The second method has been intensively developed at PSI after pioneering experiments showing that, similarly to the case of positrons, a few eV μ^+ are emitted from rare gas solids bombarded with surface muons [5] and that this process conserves the full initial polarization [6]. The emission of these so-called epithermal muons is a consequence of the suppression of electronic processes as a kinetic energy dissipating mechanism in insulators at energies of the order of the band gap energy. This leads to a large escape depth and a preferred emission of those muons, which in their statistical slowing down cascade have reached an energy of the order of 10 eV.

Based on optimized moderators as a very slow muon source, a beam of polarized muons with variable energy has been developed at PSI making the use of muons as nano-probes possible. The practical realization is discussed in detail in [7, 8]. Surface μ^+ from the intense πE3 channel at PSI are slowed down to ∼15 eV in an appropriate moderator consisting of a thin layer (few hundreds nm) of a van der Waals bound solid deposited on a thin (∼100 μm) Ag foil. The 10^{-4}–10^{-5} fraction of the incoming beam emerging as epithermal muons from the moderator are accelerated and transported by electrostatic 'einzel' lenses and a mirror to the sample, where they are focused to a circular beam spot with typical diameter of 10 mm (FWHM) slightly depending on the implantation energy. The final kinetic energy of the muons arriving at the sample may be varied over the range 0.5–30 keV by applying an accelerating or decelerating potential of up to 12 kV to the sample and up to +20 kV to the moderator. The overall time resolution (rms) for a μSR experiment is 5–10 ns depending on energy. Continuous improvement of the relevant moderator parameters such as composition, growth parameter and temperature has led to the routine use of few hundred nm s-Ar, s-N_2, or ∼1 μm s-Ne grown on a microstructured Ag foil acting as a substrate. A top layer of ∼10 nm N_2 reduces the ion background and improves the long term stability. Figure 2 shows the efficiency

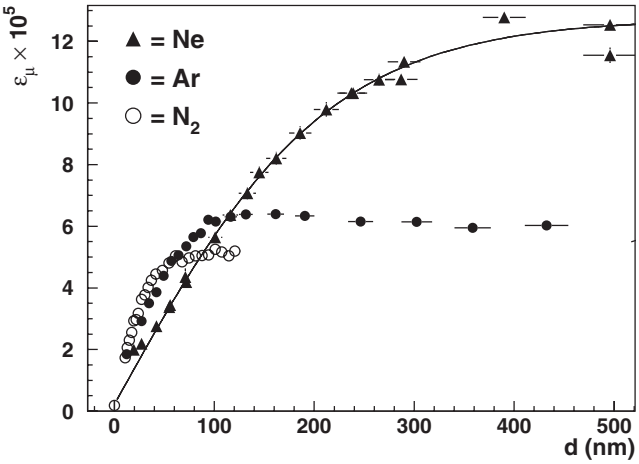

Figure 2. Moderation efficiency ε_μ—defined as the number of epithermal μ^+ divided by the number of incoming surface μ^+—for various moderating materials as a function of the thickness of the solid van der Waals layer condensed onto a patterned Ag substrate, which was held at a temperature of 6 K. The solid curve is a fit of equation (1) to the s-Ne data.

Table 1. Moderation efficiencies for solid gas moderators relative to s-N_2. With the LE-μSR setup at PSI in the πE3 area we measured ε_μ(s-N_2) $\sim 5 \times 10^{-5}$ at a beam momentum of 27.4 MeV/c and a beam momentum spread of 4% FWHM.

Moderator	Relative moderation efficiency	Escape depth (nm)
s-N_2	1.0	16
s-Ar	1.25	30
s-Ar + 12 nm s-N_2	1.42	30
s-Ne	2.5	105
s-Ne + 12 nm s-N_2	2.5	105

of various moderators as a function of the condensed van der Waals gas layer thickness. The slow muon yield increases with increasing thickness until it saturates at values of about three times the typical escape depth $L_{\rm esc}$ where—in a simple one-dimensional diffusion model—the thickness dependence of the moderation efficiency ε_μ is given by

$$\varepsilon_\mu(d) = C \cdot L_{\rm esc} \cdot \tanh\left(\frac{d}{2L_{\rm esc}}\right) + \varepsilon_0, \tag{1}$$

with d the thickness of the film, C a pre-factor proportional to the stop density of the muons and ε_0 is the efficiency of the blank substrate.

A comparison between different moderators, see table 1, shows that s-Ne is the best muon moderator. It yields an epithermal muon rate of about 3000 s^{-1} emerging from the moderator at a surface muon rate of about 2.5×10^7 s^{-1} in the πE3 area (obtained with a primary proton current of 1.8 mA impinging on a 60 mm graphite target). This results in a LE-μ^+ rate of about 1200 s^{-1} at the sample.

3. Measurements of depth profiles of low-energy muons

In contrast to conventional μSR experiments, knowledge of the implantation range and straggling at low energy is essential for designing and analysing thin film, multilayer and surface

experiments with epithermal muon beams. When the muon enters a solid sample the initial kinetic energy, which is much larger than the thermal energy of diffusion, is dissipated within a few ps. It continuously loses energy predominantly by electronic collisions and changes direction mainly by Coulomb scattering with the target nuclei. Due to the random nature of the collisions a stopping profile $n(z, E)$ is obtained as a result of the thermalization process of a muon ensemble of energy E (z depth from the sample surface). First moment and rms of this distribution are shown in figure 1 for μ^+ stopping in the high temperature superconductor $YBa_2Cu_3O_{7-\delta}$. The first quantity represents the projection to the beam direction of the total distance travelled (projected range, R_p) and the second the corresponding straggle (ΔR_p). The curves shown in figure 1 have been obtained from the moments of implantation profiles calculated by using Monte Carlo codes originally developed for protons and heavy ions and taking into account the typical finite energy resolution of the impinging beam. At low energies the profile width is typically 5–10 nm. Even for perfectly monoenergetic particles there is an inherent limit to the depth resolution due to the statistical broadening of the μ^+ implantation profile. This intrinsic broadening is the dominant effect for μ^+ of an energy larger than $\approx$2 keV (see figure 1). In the simulation the muon is treated as a hydrogen-like projectile of mass $m_\mu \cong 1/9\, m_p = 0.113$ amu. Its trajectory is calculated step by step by assuming that it changes direction with each elastic binary collision with the atom nucleus and moves in a straight free path between collisions, losing energy via inelastic electronic processes independent of elastic contributions. When the energy of the muon drops below some threshold, it stops and the projected end point of the trajectory is added in a histogram representing the range profile. These programs have been successfully tested as basic analysis tools in various solid state techniques like Rutherford backscattering, nuclear reaction analysis (e.g. for hydrogen depth profiling), elastic recoil detection analysis, secondary ion mass spectroscopy, and in many more. However, for an unrestricted use of muons as depth dependent magnetic microprobes it is indispensable to independently test whether the implantation of these particles can be reliably predicted as a function of energy for targets of variable composition and structure.

In first studies we measured partial integrals of range distributions $N(d, E) = \int_0^d n(z, E)\, dz$ in thin ($d \leqslant 100$ nm) metallic films of Al, Cu, Ag and Au evaporated on an insulating substrate (fused quartz) as a function of the implantation energy (0.5 keV $\leqslant E \leqslant$ 30 keV) and compared them with predictions from Monte Carlo codes [9]. The stopping probability of the muon in a specific layer can be determined by muon spin precession techniques using the fact that muons thermalize in metals as 'free' particles whereas in insulators they mostly form muonium. These two states can be easily distinguished by their different Larmor frequency in an external magnetic field with the amplitudes of the frequencies being directly proportional to the fraction of muons stopped in the corresponding layer. This way the quantity $N(d, E)$ and also the fraction of μ^+ backscattered from the surface as a function of the energy and target atomic number has been obtained. They are well reproduced by the simulated integrals of implantation profiles and reflection probabilities of keV muons in metals obtained with `TRIM.SP` (transport and range of ions in matter) [10] using velocity-scaled proton electronic stopping powers and energy scaled nuclear energy losses.

We recently extended the use of the muon spin rotation technique to directly image the full differential implantation profile $n(z, E)$ in a single implantation and imaging experiment. In analogy with the magnetic resonance imaging technique this quantity can be obtained from the spectrum of the Larmor precession frequencies in an inhomogeneous transverse magnetic field $B(z)$ of known gradient applied to the sample. The local magnetic field at each stopping site causes a corresponding precession of the muon spin. The temporal evolution of the polarization of the implanted muons, $P(t)$, is indicated by the positron intensity variation with time at fixed detector positions. These spectra contains oscillations which directly reflect the distribution

of local magnetic fields $p(B)$ (or of Larmor frequencies, $\omega_\mu = \gamma_\mu B$):

$$P(t) = \int_0^\infty p(B)\cos(\gamma_\mu B t + \phi)\,\mathrm{d}B. \tag{2}$$

This expression shows that $p(B)$ can be obtained by Fourier transform of the collected spectra. The field distribution sensed by the muons distributed over a profile $n(z, E)$ is connected to this quantity by the relationship

$$n(z, E)\,\mathrm{d}z = p(B, E)\,\mathrm{d}B \tag{3}$$

which states that the probability that a muon will experience a field in the interval $[B, B + \mathrm{d}B]$ is given by the probability that it will stop at a depth in the range $[z, z + \mathrm{d}z]$. Rewriting equation (3) as

$$n(z, E) = p(B, E)\frac{\mathrm{d}B}{\mathrm{d}z} \tag{4}$$

shows that the differential distribution can be determined if a sufficiently large and known magnetic field gradient is applied over the range profile. This principle has been demonstrated by a measurement of the Gaussian stopping profile of surface muons in a millimetre thick metallic foil. The relatively modest field gradient of the order of a few tens of T m^{-1}, which is required in this case was created by driving an intense electric current in the sheet [11]. Of more interest is the application of this principle to the case of LE-μ^+ where the non-Gaussian shape of the range profile is a relevant input parameter for the data analysis. Due to the reduced values of R_p and ΔR_p sizeably larger field gradients are necessary. For this we make use of the magnetic field exponentially penetrating the surface of an extreme type-II superconductor in the Meissner state $[B(z) = B_\mathrm{ext}\exp(-z/\lambda)]$. With typical values of $B_\mathrm{ext} \cong 10$ mT and $\lambda \approx 100$ nm, field gradients $B_\mathrm{ext}/\lambda \approx 10^5$ T m^{-1} can be generated within the range distribution of LE-μ^+.

Measurements have been performed on a 50 mm diameter, 700 nm thick, high quality $YBa_2Cu_3O_{7-\delta}$ (YBCO) film (thickness uniformity better than 1%), grown by thermal co-evaporation of the constituents onto a single crystal $LaAlO_3$ substrate. The transition temperature T_c was measured by ac susceptibility to be 87.5 K. The film had the crystal c-axis perpendicular to the plane and the twinned a/b planes were well orientated with the substrate. The sample was mounted in the UHV system of the slow muon source on the cold finger of a continuous flow cryostat via a sapphire plate. The YBCO film was cooled below T_c in zero field, and then a field of 9.5 mT was applied parallel to the surface and perpendicular to the muon spin thus establishing the Meissner phase. In this case, currents flowing in the ab planes determine the attenuation of the applied field into the film along the crystal c-axis. We implanted μ^+ at different energies corresponding to stopping distributions ranging from 0 to ~200 nm. The distribution of the values of magnetic field $p(B)$ experienced by the implanted muons is derived by maximum entropy Fourier analysis of the decay positron histograms [12]. Please note that in a previous experiment we assumed the knowledge of the implantation profile to microscopically prove that the field is penetrating exponentially and to make an absolute measurement of the London penetration depth and its temperature dependence [13]. Here, by contrast, we assume an exponentially decaying magnetic profile with known λ_{ab} to measure the depth profile. The argument is non-circular since for the present analysis we determine the value of λ_{ab} by an independent measurement in the vortex state. The latter is obtained by turning the external magnetic field and applying it parallel to the c-axis of the same YBCO film but perpendicular to the initial muon spin polarization so that a transverse field arrangement different from the previous one is obtained. The magnetic flux penetrates the type-II superconductor in the form of a regular hexagonal lattice of flux lines each carrying

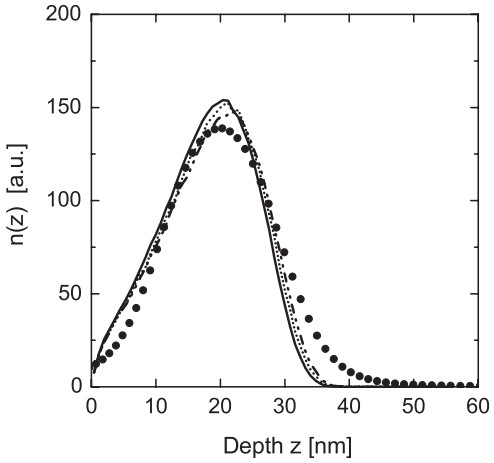

Figure 3. Implantation profile of 3.4 keV muons in YBCO obtained by the direct imaging technique (circles). The profile is compared with predictions of Monte Carlo calculations using the code `TRIM.SP` with different assumptions about the scattering potential.

one flux quantum $\Phi_0 = 2.07 \times 10^{-15}$ T m^2 resulting in a spatially varying field $\boldsymbol{B}(\boldsymbol{r})$ and a corresponding strongly asymmetric field distribution $p_{\text{vortex}}(B)$. The parameter λ_{ab} can be extracted from the difference between the mean field $\langle B \rangle = \int B p_{\text{vortex}}(B)\, \mathrm{d}B$ and the most probable field B_{saddle} of the field distribution or by fitting the field distribution to a modified London model. For the chosen geometry $\langle B \rangle = \mu_0 H_{\text{ext}}$ and a reliable estimate is given by [14]:

$$B_{\text{ext}} - B_{\text{saddle}} = \ln(2)\frac{2}{3}\frac{\Phi_0}{4\pi\lambda_{ab}^2} \tag{5}$$

from which we obtain $\lambda_{ab}(20\ \text{K}) = 150$ nm. From the simultaneous fit of $p_{\text{vortex}}(B)$ measured at different implantation energies we obtain $\lambda_{ab}(20\ \text{K}) = 145 \pm 5$ nm [15]. For the determination of $n(z, E)$ via (4) we used the latter value and included a dead layer $z_0 = 9.5$ nm [13]. The value of λ_{ab} is in good agreement with the results from microwave transmission experiments on YBCO thin films [16] and muon spin rotation measurements on YBCO single crystals [17].

Figure 3 shows as an example the depth profile of muons implanted at 3.4 keV measured by the direct imaging technique described. The curve is compared with predictions of a simulation using the code `TRIM.SP`. It can be seen that the experimental points in figure 3 are well reproduced by the calculations, with no adjustable parameters. Consistently with the results obtained in the measurements of the partial integrals, the `TRIM.SP` code gives more reliable predictions than its variant SRIM2003 [18]. The position of the most probable depth and the initial shape of the distribution are particularly well reproduced. The range profiles vary by less than 5% in the relevant range when the Moliere potential used to describe the scattering of the muons inside the solid is replaced by another elastic scattering potential. The shape of the measured profile shows deviations from the calculated distributions only at the end of the muon paths, where channelling effects and an underestimation of the finite resolution of the maximum entropy method may play a role. Overall, these and the other data show that we are able to predict the implantation profiles of low energy muon in samples with good accuracy, sometimes a necessary condition for a proper interpretation of the data.

4. Magnetic field penetration at the surface of superconductors

Often the magnetic state at the surface of a system is expected to differ from that of the bulk. An example is for instance the predicted spontaneous magnetization at the surface of a superconductor as a consequence of broken time reversal symmetry [19]. The determination of the value of a magnetic field as a function of depth below the surface is a non-trivial problem because a local probe is required to sample the local field in this region.

To illustrate the near surface sensitivity of LE-μSR we consider here the Meissner effect. In a superconductor in the Meissner state an applied field is excluded from the bulk and will penetrate only in a near surface region. In the so-called London limit [20], for a plane superconducting surface, the functional form of the decaying magnetic field $B(z)$ is predicted to be exponential, with the decay length determined by a single parameter, the London penetration depth λ_L. If the second fundamental length scale in a superconductor, the coherence length ξ, which is roughly speaking the size of a Cooper pair, is non-negligible, the electrodynamical response of the superconductor has to be averaged over it [21]. One consequence of this non-local response is the modification of the $B(z)$ dependence in the Meissner state so that for a plane superconducting surface, $B(z)$ will no longer be exponential and even change its sign beneath the surface of the superconductor. These findings were confirmed by the microscopic BCS theory [22] a few years later. Though the theoretical predictions have stood for half a century, the direct experimental verification of the functional form of $B(z)$ in the general as well in the local limit still wait for confirmation. Also a truly direct determination of the fundamental characteristics lengths of a superconductor has not been available up to now.

Common methods to measure λ_L are μSR measurements in the bulk of the vortex state [17], two-coil mutual induction techniques [23, 24], microwave experiments [25] and magnetization measurements [26, 27]. However, they rely in one way or another on model calculations or normalizations to normal state parameters and cannot be considered absolute and model independent. Bulk-μSR measurements are only applicable to type-II superconductors, since they determine λ_L from the vortex state, as previously described. They rely on the establishment of a regular vortex lattice of known symmetry where disorder is not allowed to play a dominant role. Furthermore the magnetic field generated by a single vortex must be known. Non-local effects have been sought in various other experiments: Sommerhalder and co-workers detected the sign reversal of $B(z)$ by measuring the field leaking through a hollow cylindrical film of tin [28–30]. However, no quantitative results could be drawn from this experiment. Other experiments were based on the magnetoabsorption resonance spectroscopy technique [31]. The technique uses the fact that in a type-I superconductor in a static magnetic field quasiparticle excitations are bound to the surface within the penetration layer by an effective magnetic potential of the form [32]:

$$V(z) = -\frac{e\hbar p_F}{m^*}\frac{dB}{dz} \tag{6}$$

where p_F is the Fermi momentum and m^* the effective mass of the charge carriers. Indication of non-local effects in Al was inferred by comparing microwave induced resonant transitions between the energy levels of these bound states with transition fields calculated from the energy levels of the trapping potential, parameterized to include the shape of the non-local BCS-like potential. Due to the resonant character of the experiment, only a few specific points of the potential are probed. In addition the analogous surface wells and resonances in the normal metallic state have to be understood very well in order to interpret the data. This, together with simplifications in modelling the energy levels and wavefunctions of the surface bound states, leaves room for speculation. Quasiparticle-magnetospectroscopy probes the vector potential, whereas the specular reflectivity of neutrons spin polarized parallel or anti-parallel to $\boldsymbol{B}$ may

probe the magnetic field. However, this technique requires model-fitting of spin-dependent scattering intensities and does not give a direct measure of the spatial variation of the magnetic field. Experiments performed so far have found non-local effects to lie beyond the sensitivity of polarized neutron reflectivity [33].

For a theoretical description of the Meissner–Ochsenfeld effect one has to take into account that an external electromagnetic field acts on the ground state of a superconductor as a perturbation[4]. Within a standard perturbation expansion one can show [34] that the following non-local relation between the current density $\boldsymbol{j}$ and the vector potential $\nabla \wedge \boldsymbol{A} = \boldsymbol{B}$ holds in the stationary case:

$$j_\alpha(\boldsymbol{r}) = -\sum_\beta \int \underbrace{\left\{ R_{\alpha\beta}(\boldsymbol{r}-\boldsymbol{r}') - \frac{e^2 n_S}{m^*}\,\delta(\boldsymbol{r}-\boldsymbol{r}')\delta_{\alpha\beta} \right\}}_{=:K_{\alpha\beta}(\boldsymbol{r}-\boldsymbol{r}')} A_\beta(\boldsymbol{r}')\,\mathrm{d}\boldsymbol{r}' \tag{7}$$

where e is the electron charge and n_S the supercarrier density. $K_{\alpha\beta}(\boldsymbol{r}-\boldsymbol{r}')$ is called the integral kernel. The vector potential $\boldsymbol{A}(\boldsymbol{r})$ needs to be properly gauged so that equation (7) is physically meaningful[5]. $R_{\alpha\beta}(\boldsymbol{r}-\boldsymbol{r}')$ describes the (non-local) paramagnetic response, whereas the second term in the bracket reflects the diamagnetic one. If the ground state wavefunction of the superconductor were 'rigid' with respect to all perturbations $R_{\alpha\beta}$ would be identically zero and equation (7) would reduce to the London equation

$$j_\alpha(\boldsymbol{r}) = -\frac{1}{\mu_0}\frac{1}{\lambda_L^2} A_\alpha(\boldsymbol{r}) \tag{8}$$

with the London penetration depth $\lambda_L = \sqrt{m^*/(\mu_0 e^2 n_S)}$ and μ_0 the permeability of the vacuum. This, together with the Maxwell equation $\nabla \wedge \boldsymbol{B} = \mu_0 \boldsymbol{j}$, results, for a semi-infinite sample, in the well known penetration profile

$$B(z) = B_{\mathrm{ext}} \exp(-z/\lambda_L), \tag{9}$$

where B_{ext} is the externally applied magnetic field.

In situations where the paramagnetic term $R_{\alpha\beta}$ in equation (7) cannot be neglected one arrives by using the Fourier transform of equation (7) to the expression (in the one dimensional case of specular reflection of the charge carriers at the surface)

$$B(z) = B_{\mathrm{ext}} \int \frac{q}{q^2 + \mu_0 K(q\xi, T, \ell)} \sin(qz)\,\mathrm{d}q, \tag{10}$$

where $K(q\xi, T, \ell)$ is the Fourier transformed kernel from equation (7). It can be expressed explicitly in the Pippard model [21] or a microscopic theory such as BCS [22]. Equation (10) reduces to an exponential decay if $K(q\xi, T, \ell)$ is independent of q, and indeed, in the London limit $\mu_0 K(q\xi, T, \ell) = 1/\lambda_L^2$. ℓ is the electronic mean free path and $\xi(T, \ell)$ the Pippard coherence length:

$$\frac{1}{\xi(T,\ell)} = \frac{J(0,T)}{\xi(0)} + \frac{1}{\ell} \tag{11}$$

with the weak temperature dependence of $\xi(T, \ell)$ given by BCS theory

$$J(0,T) = \left[\frac{\lambda(T)}{\lambda(0)}\right]^2 \frac{\Delta(T)}{\Delta(0)} \tanh\left[\frac{\Delta(T)}{2k_B T}\right], \tag{12}$$

where $\Delta(T)$ is the superconducting energy gap and k_B the Boltzmann constant.

[4] This is at least true for magnetic field strength $H \ll H_c$ (H_c, thermodynamical critical field) and for frequencies $\nu \ll 2\Delta/\hbar$, where Δ is the energy gap and $\hbar$ the Planck constant divided by 2π.

[5] The gauge invariance requires $\nabla \cdot \boldsymbol{A} = 0$, i.e. only the transverse part of $\boldsymbol{A}$ has to be used.

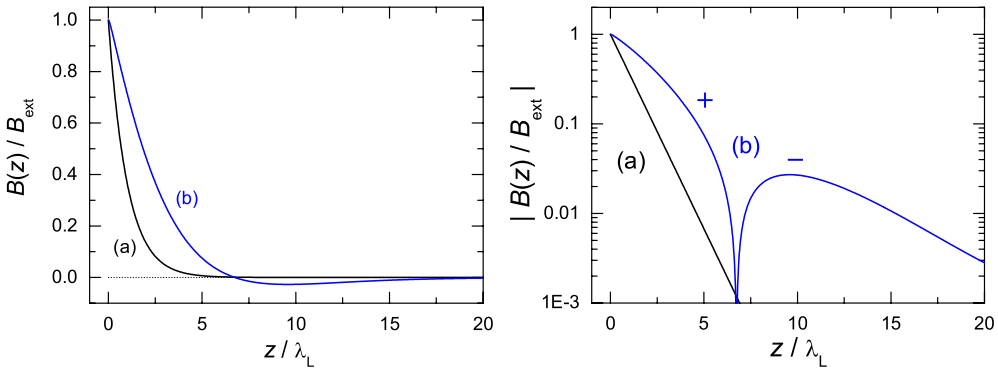

Figure 4. Theoretical magnetic penetration profiles in the Meissner state for (a) a hypothetical material in the London limit ($\xi \ll \lambda_L$) with $\lambda_L = 50$ nm, and (b) aluminium according to equations (10)–(12) for $\xi(0) = 1600$ nm and $\lambda_L = 50$ nm.

Type-I superconductors require a non-local treatment. However, it should be noted that the border between type-I and II superconductors ($\kappa \equiv \lambda_L/\xi = 1/\sqrt{2}$) does not coincide with the border between local and non-local electrodynamics and that in isotropic superconductors noticeable non-local effects are expected for κ as large as 1.6 [35].

Even in extreme type-II superconductors such as the high-temperature superconductors subtle non-local effects are predicted if the superconducting ground state has a gap with nodes [36]. Close to these points of the Fermi surface the anisotropic coherence length $\xi(k) = \hbar v_F/(\pi \Delta_k)$ effectively diverges and therefore equation (7) becomes angular dependent with local and non-local contributions. The functional form of equation (10) is valid even in the strong coupling limit, if ξ and λ_L are properly renormalized: $\xi \to \xi/\sqrt{Z}$ and $\lambda_L \to \lambda_L Z$ with $Z = 1 + \lambda_{e-ph}$ (λ_{e-ph}, electron–phonon coupling) [37].

Figure 4 shows magnetic penetration profiles in the Meissner state for a plane superconductor surface calculated for the local case (a) and an extreme non-local case (b). Note the different shape of $B(z)$: in the local case the initial slope is larger, i.e. the magnetic field penetrates less deeply into the superconductor reflecting the more efficient diamagnetic screening. In the logarithmic plot the non-local penetration profile shows a clear deviation from an exponential shape, exhibiting a sign reversal of the field at some distance from the interface.

As an example of magnetic field profiling we present selected data of YBCO and Pb. These two materials were chosen since YBCO is a clear cut type-II superconductor ($\lambda_L \gg \xi$) which should show an exponential decaying magnetic penetration profile[6], whereas Pb in the clean limit should show a clear non-exponential $B(z)$ according to equation (10). For detailed discussion and other materials investigated by the same technique, we refer the reader to [13, 38, 39]. The characterization of the YBCO sample was presented in section 3. The Pb sample was directly sputtered onto a sapphire crystal (diameter 50 mm). The thickness of the film was determined by a high sensitivity surface profiler and Rutherford backscattering (RBS) to $d = 1055(50)$ nm. An oxide layer of 5.8(3) nm was measured by RBS. The critical temperature, $T_c = 7.21(1)$ K, was measured by means of resistivity and susceptibility measurements. From resistivity data a mean free path $\ell \approx 100$ nm was estimated. The experiments were carried out in transverse field geometry. A field B_{ext} of typically 0.1 mT was applied parallel to the sample surface after zero field cooling. B_{ext} was chosen to be much

[6] Non-local effects predicted in this material due to the d-wave character manifest themselves primarily in the T-dependence of λ at very low temperatures ($T \ll 1$ K) and for $B_{ext} \parallel c$-axis.

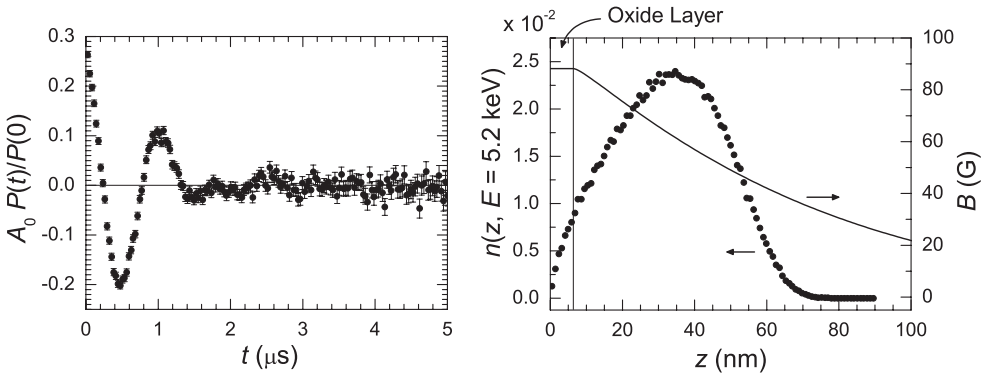

Figure 5. Typical time spectrum $A_0 P(t)/P(0)$ of a LE-μSR experiment. The data shown are from Pb, zero field cooled, $T = 3.05$ K ($T_c = 7.21$ K), $B_{ext} = 8.82(6)$ mT, and an implantation energy $E = 5.2$ keV. The right-hand side shows the μ^+ stopping distribution $n(z, E = 5.2\ \text{keV})$ for Pb and the magnetic penetration profile.

smaller than the thermodynamic critical field H_c for Pb and $B_{ext} \ll H_{c_1}$, the lower critical field for YBCO. Muons were implanted in the sample with variable energy between 1 and 30 keV and having their initial spin direction parallel to the surface and perpendicular to B_{ext}. The value of the applied magnetic field was determined from the Larmor frequency measured at a temperature above T_c.

A typical LE-μSR time spectrum $A_0 P(t)/P(0)$ for Pb in the Meissner state is shown in figure 5. A_0 is the experimental asymmetry and $P(t)/P(0)$ the normalized μ^+ spin polarization. The right-hand side shows the corresponding μ^+ stopping distribution, $n(z, E)$, as well as the expected magnetic field profile. In the experiments with LE-μ^+ magnetic field distributions $p(B, E)$ as a function of the implantation energy E are measured. The starting equation to relate this quantity to the spatial variation of the local field is equation (3), which integrated on both sides yields:

$$\int_0^z n(\zeta, E)\,\mathrm{d}\zeta = \int_B^\infty p(\beta, E)\,\mathrm{d}\beta. \tag{13}$$

Since $n(z, E)$ can be simulated very reliably (see section 3) equation (13) represents for a given z an equation for B from which the functional relationship $B(z)$ is obtained. An important point to be noted is that the physical processes simulated in `TRIM.SP` are absolutely unrelated to any theory or model describing superconductivity and hence $B(z)$ is obtained without any previous *a priori* assumption about the superconducting state. This is an important difference with respect to other methods to determine for instance the penetration depth. Figure 6 shows measured magnetic penetration field profiles $B(z)$ for Pb and YBCO plotted as reduced field $B(z)/B_{ext}$ versus z/λ_L. The small symbols which form an almost dense curve show magnetic field profiles obtained via equation (13). The circles with the error bars originate from an alternative way to analyse the data making use of the moments of the distributions and an iterative procedure starting from equation (3) (see [13, 38]). The profile in YBCO follows the exponential law as predicted by equation (9) with a magnetic penetration depth $\lambda_L^{YBCO} = 146(3)$ nm at 20 K. In contrast, the magnetic field profile for Pb strongly deviates from an exponential curve and displays the characteristic curvature predicted by equation (10). Unfortunately, due to the present energy range of the muons, we could not follow $B(z)$ to very low fields, which would allow us to test the field reversal beneath the surface. Fits with the BCS theory yield a magnetic penetration depth of $\lambda_L^{Pb} = 55(1)$ nm and a coherence length $\xi^{Pb}(0) = 90(5)$ nm at $T = 0$ K.

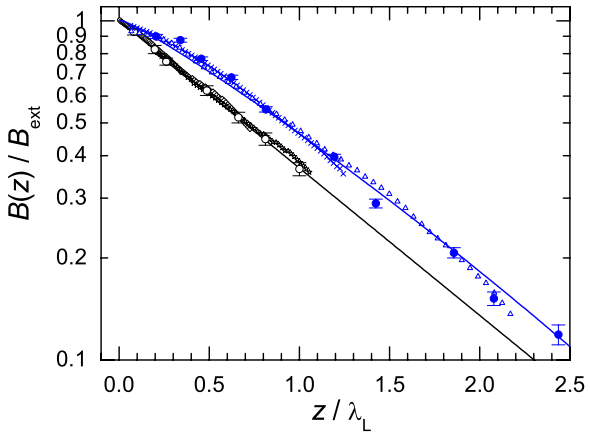

Figure 6. Magnetic penetration profile in the Meissner state. Lower data set: $YBa_2Cu_3O_{7-\delta}$ at $T = 20$ K ($T_c = 87.5$ K); upper data set: Pb at $T = 3.05$ K ($T_c = 7.21$ K). The curves are fits to the corresponding models. For details see the text.

These two experiments exemplarily demonstrate the ability of the LE-μSR technique to image magnetic field profiles beneath the surface of materials on a nanometre length scale and to yield a direct determination of otherwise not easily accessible quantities such as magnetic penetration depth and coherence length. The magnetic penetration depth is related via $\lambda_L \propto \sqrt{m^*/n_S}$ to fundamental parameters of the superconducting carriers and has provided detailed information about microscopic characteristics of the superconducting state (for instance about the gap symmetry via its T-dependence [40]). The fact that this quantity as obtained from the microscopic profile in the Meissner state is not obscured by normalizations or details of the vortex state (as in μSR experiments based on relationships between field inhomogeneities in the mixed state and λ_L) makes this method very well suited for searches for delicate effects where a precise determination of λ_L is crucial. One example is the search for isotope effects in high-temperature superconductors [41]. Very recently, the magnetic field profiles in the Meissner state of nearly optimally doped YBCO films with ^{16}O and ^{18}O substituted atoms were measured by means of LE muons. While a small isotope effect on T_c was observed, a significant relative difference of 2.8% could be detected in the in-plane magnetic penetration depth λ_{ab}, i.e. of 5.6% in m^*_{ab}, respectively [27]. This result indicates that in optimally doped cuprate superconductors, even if a small isotope effect on T_c is observed, the mass of the superconducting carriers is not decoupled from the mass of the lattice atoms, which is not expected in a BCS model as long as the adiabatic approximation holds, which is the case for most classical superconductors.

5. Interlayer exchange coupling in Fe/Ag/Fe trilayers—mapping the spin polarization in the Ag spacer

Controlling thin film growth on a nanometre scale has opened the possibility of tailoring magnetic heterostructures with new fascinating physical properties. The combination of different materials and the small dimensions of these heterostructures lead to the extraordinary properties of artificially layered systems including spin transport [42, 43], giant magnetoresistance (GMR) [44, 45] and interlayer exchange coupling (IEC) [46]. The IEC between two ferromagnetic films separated by a non-magnetic spacer oscillates and changes sign as a function of spacer thickness. Theoretical models imply the existence of a spatially

oscillating conduction electron spin polarization in the spacer which mediates the magnetic coupling. This quantity is hardly accessible experimentally since the small induced polarization rapidly decays as a function of distance from the magnetic interface and since the non-magnetic layer is sandwiched between the ferromagnetic layers with large magnetic moments. Therefore a local probe with large sensitivity is needed to investigate these systems. LE-μSR has allowed us for the first time to determine the induced conduction electron spin polarization in the Ag spacer of an epitaxial 4 nm Fe/20 nm Ag/4 nm Fe(001) trilayer at large distances x from the magnetic interface.

The most intuitive approach to describe the IEC is the so-called Ruderman–Kittel–Kasuya–Yosida (RKKY) model, originally developed to describe the indirect coupling of localized magnetic impurities embedded in a non-magnetic metallic host [47, 48]. Here the coupling between the magnetic ions is mediated by a spatially oscillating conduction electron spin polarization of the metal with strength and sign of the coupling determined by the direct exchange interaction between the conduction electrons and the impurity spin and by the distance R of the magnetic ions. In a free-electron approximation, the exchange integral $J(R)$ oscillates according to

$$J(R) \propto \frac{2k_{\mathrm{F}}R\cos(2k_{\mathrm{F}}R) - \sin(2k_{\mathrm{F}}R)}{(2k_{\mathrm{F}}R)^4}, \tag{14}$$

with k_{F} the Fermi vector of the host material. By proper summation of the RKKY interaction over the two magnetic sheets separated by a metallic spacer of thickness D this model can be adopted to describe the IEC in a straightforward manner [49–51]. The interlayer coupling energy E_{i} per unit area can be written as

$$E_{\mathrm{i}} = -J(D)\frac{\boldsymbol{M}_1 \cdot \boldsymbol{M}_2}{M_1 M_2} \tag{15}$$

with M_i the magnetization of the two ferromagnetic layers and $J(D)$ the coupling constant, which oscillates with the spacer thickness:

$$J(D) \propto D^{-2}\sin(2k_{\mathrm{F}}D). \tag{16}$$

The R^{-3} decay for isolated magnetic ions modifies to a D^{-2} dependence in the IEC case as a consequence of the integration over the magnetic sheets. It should be noted that this simple model only predicts one oscillation period $\Lambda = \pi/k_{\mathrm{F}}$ of the order of the lattice constant. Experiments determining the IEC strength, however, often observe two oscillations with much larger period [52]. This can be understood by taking into account real non-spherical Fermi surfaces and the fact that in experiments with variable spacer thickness the IEC is sampled in steps of one monolayer.

The oscillation periods are determined by the topology of the Fermi surface of the spacer [53, 54]. In particular, parallel regions of the Fermi surface connected by extremal spanning vectors q perpendicular to the interface dominate the coupling due to their high density of electronic states. Multiple extremal spanning vectors lead to a superposition of oscillations with different periods. Figure 7 shows a sketch of the Ag Fermi surface. Two extremal spanning vectors along the [001] direction are present in Ag: one at the belly (q_{belly}) and one at the neck (q_{neck}) of the Fermi surface. Sampling the oscillating function with the wavenumber q at discrete points results in an observable oscillation periods Λ that can be remarkably larger than the lattice constant [49]. Due to this aliasing effect, e.g. effective oscillation periods $\Lambda_{\mathrm{belly}} = 1.17$ nm and $\Lambda_{\mathrm{neck}} = 0.485$ nm have been observed in Fe/Ag/Fe [55] in excellent agreement with the ones calculated from the Ag Fermi surface [53]. In summary, if both the non-spherical Fermi surfaces and the aliasing effect are taken into account, equation (16)

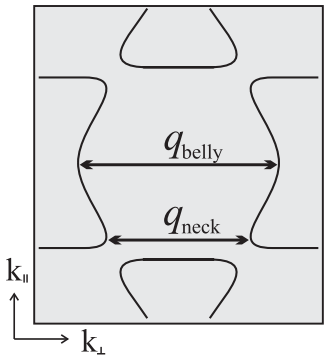

Figure 7. Sketch of the (001) Ag Fermi surface cross section. The two extremal spanning vectors at the belly and at the neck of the Fermi surface dominate the IEC and give rise to the observed long and short period oscillations, respectively.

generalizes to

$$J(D) \propto \sum_n C_n D^{-2} \sin(2\pi D/\Lambda_n + \phi_n), \tag{17}$$

where the sum is performed over all extremal spanning vectors with the corresponding effective oscillation periods. In this extended RKKY model, the amplitudes C_n do not only depend on the contact interaction of the conduction electrons to the ferromagnetic ions, but also on the curvature of the Fermi surface at the corresponding extremal points. The phases ϕ_n are determined by the type of the extremal spanning vector, with ϕ_n equal to 0, $\pi/2$, or π, when q_n is a maximum, a saddle point, or a minimum, respectively. Various experiments probing the relative orientation of the magnetization of the two ferromagnetic layers as a function of spacer thickness have shown that the RKKY theory is able to make good predictions about the oscillation periods and that it gives a relatively intuitive physical understanding of the coupling mechanism [54]. Within the RKKY theory the coupling of the ferromagnetic layers is mediated by the oscillating conduction electron polarization in the spacer. The associated local magnetization $M_{\rm loc}(x)$ is given by the superposition of the magnetization profiles $M(x)$ induced by each of the two interfaces $M_{\rm loc}(x) = M(x) + M(D - x)$

$$M(x) \propto \sum_n C_n x^{-2} \sin(2\pi x/\Lambda_n + \phi_n), \tag{18}$$

with x being the distance to the interface. Although this locally induced polarization is the essential element of the model, it had never been investigated thoroughly due to the lack of suitable experimental techniques.

The conduction electron spin polarization has been determined by LE-μSR in the Ag layer of a epitaxially grown Fe/Ag/Fe(001) trilayer [56] and in a Fe/Ag(001) bilayer [57]. The muon probes the local polarization of the conduction electrons $M_{\rm loc}(x)$ by sensing the corresponding Fermi contact field $\mu_0 M_{\rm loc}(x)$ at interstitial lattice sites. The high sensitivity of the μSR technique allows us to detect induced magnetic moments down to 10^{-4} $\mu_{\rm B}$, making it possible to study the spin polarization at much larger distances from the magnetic interface than with other local probe techniques.

Figure 8 depicts the principle of the LE-μSR measurement. Muons with a kinetic energy of 3 keV are implanted into the sample where they stop within the Ag spacer with a range distribution $n(x)$. Transverse field μSR measurements have been performed on magnetized samples, with the external field $B_{\rm ext} = 8.8$ mT applied along the magnetically easy axis of

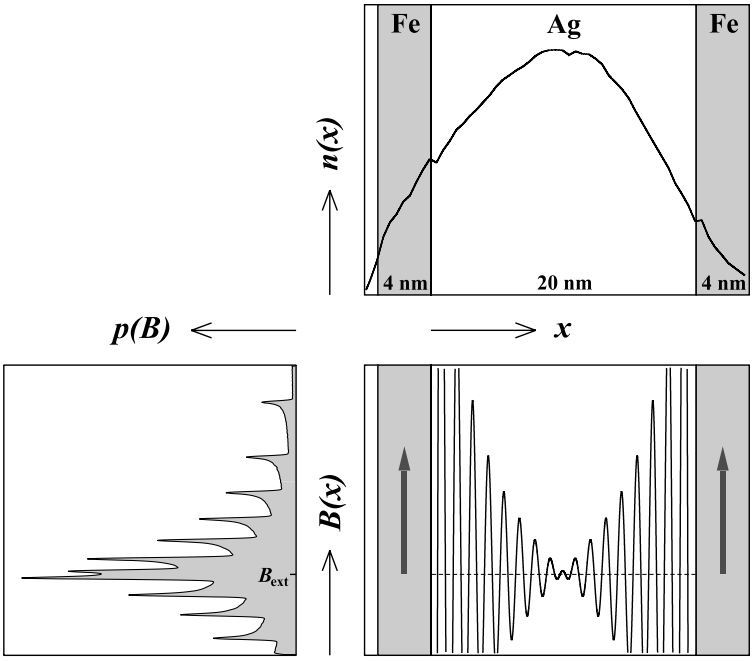

Figure 8. Principle of the LE-μSR investigation of the oscillating induced conduction electron spin polarization in the Ag spacer of a 4 nm Fe/20 nm Ag/4 nm Fe(001) trilayer. The muons are implanted into the trilayer with the stopping distribution $n(x, E)$. The measured field distribution $p(B)$ directly reflects the spatial variation of the polarization within the spacer as sampled by the muon ensemble. Negative and positive hyperfine field contributions caused by the Fermi contact interaction between the μ^+ and polarized conduction electrons add to $B_{\rm ext}$. $p(B)$ exhibits distinct peaks at values corresponding to maxima or minima of the oscillating $B(x)$.

the sample within the film plane. In this situation, the local field at the muon in silver is the sum of the external magnetic and the Fermi contact field: $B(x) = B_{\rm ext} + \mu_0 M_{\rm loc}(x)$. Since the muons are distributed over the whole spacer, the measured field distribution $p(B)$ reflects the spatial variation of the conduction electron spin polarization sampled by the μ^+ ensemble. This allows us to investigate $M_{\rm loc}(x)$ for a large portion of the spacer with a single LE-μSR experiment without the necessity to rely on several samples with different thicknesses. For a given theoretical $M_{\rm loc}(x)$, the expected field distribution $p(B)$ can be calculated by weighting $M_{\rm loc}(x)$ with the μ^+ stopping profile $n(x)$. A spatially oscillating $M_{\rm loc}(x)$, as shown in figure 8, gives rise to distinct peaks in $p(B)$. The peaks in $p(B)$ reflect the higher probability density of B at those depths x in the spacer where the oscillating $B(x)$ is maximum or minimum. It should be noted that the peaks in $p(B)$ alternate around $B_{\rm ext}$ reflecting the damped oscillation in the spacer. The peaks next to $B_{\rm ext}$ arise from the extreme values of $B(x)$ in the centre of the spacer, while the peaks further away from $B_{\rm ext}$ are due to maxima and minima which are closer to the interfaces. The actual measured field distribution $p(B)$ has been obtained from time-differential LE-μSR data in three different ways:

(i) by fitting the data directly in the time domain with a superposition of precessing signals of unknown amplitudes,
(ii) by a simple fast Fourier transformation, and
(iii) by a maximum entropy analysis.

Figure 9 shows the results from the different types of analysis.

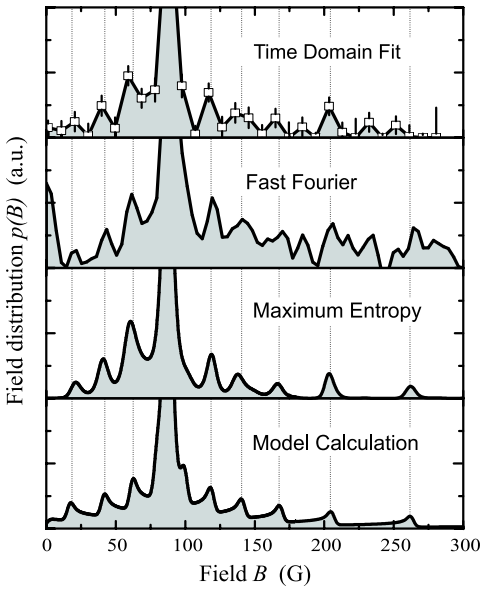

Figure 9. Field distribution $p(B)$ sensed by the μ^+ ensemble from: fit in time domain of the time-differential LE-μSR data, fast Fourier transformation and maximum entropy analysis. Independent of the analysis the distributions show the typical features of a spatially oscillating conduction electron polarization within the Ag spacer. The model calculation represents the best fit to the data. The dotted vertical lines indicate the position of the characteristic peaks in $p(B)$.

The position of the peaks reflecting the spatially oscillating M_{loc} is robust versus different methods used to extract the frequency spectrum. Independent of the analysis the data actually exhibits all the essential features expected for a spatially oscillating $M_{\mathrm{loc}}(x)$ within the spacer. The data can be best fitted by a model based on equation (18) (see figure 9). Only the long period oscillation ($\Lambda_{\mathrm{belly}} = 1.17$ nm) which corresponds to the extremal spanning vector from the belly of the Ag Fermi surface is necessary to describe the oscillating polarization and the corresponding $p(B)$. No contribution of the short period oscillation ($\Lambda_{\mathrm{neck}} = 0.485$ nm) to $M_{\mathrm{loc}}(x)$ is observed. Furthermore, the electron spin polarization of the belly states is found to be of extremely long-range nature giving rise to a $x^{-0.8(1)}$ decay of the polarization as a function of distance from the interface.

The observation of the same periodicity Λ_{belly} for the IEC and for $M_{\mathrm{loc}}(x)$ measured by LE-μSR proves their close relationship. The short period oscillation is not detected in our experiment. This is in accordance with the observation that the IEC is dominated by the belly states in the Fe/Ag/Fe system [58]. Moreover, it is reasonable to assume that, due to roughness of the interfaces and to thickness variations of the spacer which are of the same order as Λ_{neck}, the short period oscillation is washed out at the μ^+ site. However, the unexpectedly long range of $M_{\mathrm{loc}}(x)$ is at variance with the simple RKKY model, which predicts a x^{-2} dependence of the polarization. Furthermore, the IEC strength in Fe/Ag/Fe is found to follow the expected D^{-2} law [59].

A possible reason for this unexpected behaviour is the spin-dependent quantum confinement of conduction electrons within the spacer [60, 61], which is neglected by the RKKY model. Unfortunately, an analytic expression for $M_{\mathrm{loc}}(x)$ that includes the quantum confinement of electrons in the spacer is not available for the Fe/Ag/Fe system. Semi-analytical estimates exist only for Co/Cu/Co giving an asymptotic stationary phase formula for the

polarization [62]. In this model, the amplitude and the decay of the oscillating polarization depend on the curvature and velocity of carriers at the Fermi surface extremal points and on the matching of ferromagnet and spacer bands. Due to the mismatch of the conduction bands, the neck states are fully confined within the spacer in Co/Cu/Co. For the contribution of these electron states, the theory predicts a x^{-1} initial decay of the polarization and a clear deviation from the x^{-2} law for distances up to 20 nm. In Fe/Ag/Fe the belly states are fully confined as proven by photoemission spectroscopy [63]. In analogy to the Cu/Co system, it may be argued that the confined belly states in Fe/Ag could also lead to a long-range oscillating conduction electron polarization as observed by LE-μSR. The apparent difference between the IEC and the induced polarization has also been inferred from numerical calculations of the Co/Cu/Co system [64]. Here, the authors conclude that the IEC cannot be regarded as a transfer of an oscillating magnetic moment, but that it is rather caused by the energy difference due to the confined quantum well states within the spacer.

In summary, the LE-μSR data represent the first observation of the conduction electron spin polarization at large distances from the magnetic interface within a trilayer, revealing its extreme long-range nature. This unexpected behaviour might be caused by the confinement of electron states from the belly of the Ag Fermi surface. However, this conclusion is based on theoretical works for the Co/Cu system, using analogical arguments. Therefore, proper calculations for the Fe/Ag system are needed to provide further evidence for this scenario.

The investigations on the trilayer have been complemented by energy-dependent measurements on a 4 nm Fe/300 nm Ag(001) bilayer [57]. Using muon implantation energies between 3 and 30 keV, the induced conduction electron spin polarization was probed in Ag at different depths up to 107 nm beneath the magnetic interface. A long-range polarization within Ag is inferred from the measured μSR depolarization rates for the bilayer sample, thus qualitatively confirming the results obtained in the trilayer system. Very recent measurements with LE-μSR of a ferromagnet/superconductor/ferromagnet thin film hybrid structure (Fe/Pb/Fe) have shown also evidence of a long range oscillating electron spin polarization in the spacer material above and below the superconducting transition temperature. The general RKKY-type features and the attenuation coefficient are in good agreement with the ones found in the Fe/Ag/Fe system [65].

6. Outlook

The availability of 100% polarized muons of tuneable energy in the keV range has allowed the extension of μSR techniques to study thin films, multilayered samples and near surface regions. The kind of information provided by LE-μSR is hardly accessible by other methods. A similar technique is β-NMR [66], which is complementary and attractive in concomitance with μSR because longer relaxation times can be observed. Compared to more mature nuclear solid state techniques LE-μSR is still in its infancy. However, the experiments summarized in this overview well illustrate the potential to obtain a novel characterization of superconducting and magnetic properties.

Especially interesting is the possibility to directly profile local magnetic fields and spin polarizations in near surface regions or thin films on a nm scale and to study thin film heterostructures layer by layer. Multilayers, designed and produced in a huge variety of configurations, can be used to investigate for instance a long standing question such as the coexistence and interplay of magnetism and superconductivity. This can be addressed by measuring the local magnetization of heterostructures consisting of ferro-or antiferromagnetic materials and superconductors. In addition, multilayered structures of isostructural insulating, conducting and superconducting materials of the 123 compound are ideal model systems to

probe specific properties of high-T_c superconductors, such as the role of the individual layer thickness, of the coupling between superconducting layers or of the two-dimensional versus three-dimensional nature of unconventional superconductivity. LE-μSR can also expose dimensional or surface effects in many other fields (e.g. in spin glass freezing or polymer dynamics).

Last but not least we would like to mention that we expect a quantum step in the capability of LE-μSR with the completion at PSI of the new high intensity surface muon beam line, which has been specially designed for LE-μ^+ applications and is in an advanced stage of construction. Increase of the LE-μ^+ intensity by a factor of seven at the dedicated new μE4 beam line will result in a rate at the sample of about 8000 s^{-1} thus achieving fluxes which are comparable to bulk μSR facilities. This will allow the full exploitation of the potential of this novel technique.

Acknowledgments

This work was performed at the Swiss Muon Source (SμS), Paul Scherrer Institute (PSI, Switzerland). The authors are grateful to E Forgan, H Keller and J Litterst for their collaborations and useful discussions.

References

[1] Lee S, Kilcoyne S and Cywinski R (ed) 1999 *Muon Science* (Bristol: Institute of Physics Publishing)
[2] Taqqu D 1986 *Nucl. Instrum. Methods* A **247** 288
[3] Muhlbauer M, Daniel H and Hartmann H 1999 *Hyperfine Interact.* **119** 305
[4] Nagamine K, Miyake Y, Shimomura K, Birrer P, Marangos J P, Iwasaki M, Strasser P and Kuga T 1995 *Phys. Rev. Lett.* **74** 4811
[5] Harshman D R, Mills A P Jr, Beveridge J L, Kendall K R, Morris G D, Senba M, Warren J B, Rupaal A S and Turner J H 1987 *Phys. Rev.* B **36** 8850
[6] Morenzoni E, Kottmann F, Maden D, Matthias B, Meyberg M, Prokscha Th, Wutzke Th and Zimmermann U 1994 *Phys. Rev. Lett.* **72** 2793
[7] Morenzoni E *et al* 2000 *Physica* B **289/290** 653
[8] Prokscha T, Morenzoni E, David C, Hofer A, Glückler H and Scandella L 2001 *Appl. Surf. Sci.* **172** 235
[9] Morenzoni E, Glückler H, Prokscha T, Khasanov R, Luetkens H, Birke M, Forgan E M and Niedermayer Ch 2002 *Nucl. Instrum. Methods* B **192** 254
[10] Eckstein W 1991 *Computer Simulation of Ion–Solid Interactions* (Berlin: Springer)
[11] Shiroka T, Bucci C, De Renzi R, Guidi G, Eaton G, King P and Scott C 1999 *Nucl. Instrum. Methods* B **152** 241
[12] Rainford B D and Daniell G J 1994 *Hyperfine Interact.* **87** 1129
[13] Jackson T J *et al* 2000 *Phys. Rev. Lett.* **84** 4958
[14] Sidorenko A D, Smilga V P and Fesenko V I 1990 *Hyperfine Interact.* **63** 49
[15] Niedermayer Ch *et al* 1999 *Phys. Rev. Lett.* **83** 3932
[16] De Vauchier L A *et al* 1996 *Europhys. Lett.* **33** 153
[17] Sonier J E, Brewer J H and Kiefl R F 2000 *Rev. Mod. Phys.* **72** 769
[18] Ziegler J F and Biersack J P 1985 *The Stopping and Range of Ions in Solids* vol 1, ed J F Ziegler (New York: Pergamon)
[19] Sigrist M and Ueda K 1991 *Rev. Mod. Phys.* **63** 239
[20] London F and London H 1935 *Proc. R. Soc.* A **149** 71
[21] Pippard A B 1953 *Proc. R. Soc.* A **216** 547
[22] Bardeen J, Cooper L N and Schrieffer J R 1957 *Phys. Rev.* **108** 1175
[23] Jeanneret B, Gavilano J L, Racine G A, Leemann Ch and Martinoli P 1989 *Appl. Phys. Lett.* **55** 2336
[24] Turneaure S J, Ulm E R and Lemberger Th R 1996 *J. Appl. Phys.* **79** 4221
[25] Harris R, Hosseini A, Kamal S, Dosanjh P, Liang R, Hardy W W and Bonn D A 2001 *Phys. Rev.* B **64** 064509
[26] Shoenberg D 1940 *Proc. R. Soc.* A **175** 49
[27] Khasanov R *et al* 2004 *Phys. Rev. Lett.* **92** 057602

[28] Sommerhalder R and Thomas H 1961 *Helv. Phys. Acta* **34** 29
[29] Sommerhalder R and Thomas H 1961 *Helv. Phys. Acta* **34** 265
[30] Drangeid K E and Sommerhalder R 1962 *Phys. Rev. Lett.* **8** 467
[31] Doezema R E, Huffaker J N, Whitmore S, Slinkman J and Lawrence W E 1984 *Phys. Rev. Lett.* **53** 714
[32] Pincus P 1967 *Phys. Rev.* **158** 346
[33] Nutley M P, Boothroyd A T, Staddon C R, Paul D MK and Penfold J 1994 *Phys. Rev.* B **49** 15789
[34] Schrieffer J R 1964 *Theory of Superconductivity* (San Francisco, CA: Addison-Wesley)
[35] Halbritter J 1971 *Z. Phys.* **243** 201
[36] Kosztin I and Leggett A J 1997 *Phys. Rev. Lett.* **79** 135
[37] Nam S B 1967 *Phys. Rev.* **156** 470
[38] Suter A, Morenzoni E, Khasanov R, Luetkens H, Prokscha T and Garifianov N 2004 *Phys. Rev. Lett.* **92** 087001
[39] Suter A, Morenzoni E, Garifianov N, Khasanov R, Kirk E, Luetkens H, Prokscha T and Horisberger M 2004 unpublished
[40] Hardy W N, Bonn D A, Morgan D C, Liang R and Zhang K 1993 *Phys. Rev. Lett.* **70** 3999
[41] Khasanov R, Shengelaya A, Morenzoni E, Conder K, Savic I M and Keller H 2004 *J. Phys.: Condens. Matter* **16** S4439
[42] Prinz G A 1995 *Phys. Today* **48** 58
[43] Kikkawa J M and Awschalom D D 1999 *Nature* **397** 139
[44] Baibich M N, Broto J M, Fert A, Van Dau F N and Petroff F 1988 *Phys. Rev. Lett.* **61** 2472
[45] Binasch G, Grünberg P, Saurenbach F and Zinn W 1989 *Phys. Rev.* B **39** 4828
[46] Grünberg P, Schreiber R, Pang Y, Brodsky M B and Sowers H 1986 *Phys. Rev. Lett.* **57** 2442
[47] Ruderman M A and Kittel C 1954 *Phys. Rev.* **96** 99
[48] Yosida K 1957 *Phys. Rev.* **106** 893
[49] Coehoorn R 1991 *Phys. Rev.* B **44** 9331
[50] Yafet Y 1987 *Phys. Rev.* B **36** 3948
[51] Baltensperger W and Helman J S 1990 *Appl. Phys. Lett.* **57** 2954
[52] Bürgler D E, Grünberg P, Demokritov S O and Johnson M T 2001 *Interlayer Exchange Coupling in Layered Magnetic Structures* (*Handbook of Magnetic Materials* vol 13) ed K H J Buschow (Amsterdam: Elsevier Science B.V.) chapter 1, pp 1–85
[53] Bruno P and Chappert C 1991 *Phys. Rev. Lett.* **67** 1602
[54] Bruno P and Chappert C 1992 *Phys. Rev.* B **46** 261
[55] Unguris J, Celotta R J and Pierce D T 1993 *J. Magn. Magn. Mater.* **127** 205
[56] Luetkens H *et al* 2003 *Phys. Rev. Lett.* **91** 017204
[57] Luetkens H, Korecki J, Morenzoni E, Prokscha T, Suter A, Birke M, Garifianov N, Khasanov R, Ślezak T and Litterst F J 2003 *J. Magn. Magn. Mater.* **272–276** 1128
[58] Unguris J, Celotta R J, Tulchinsky D A and Pierce D T 1999 *J. Magn. Magn. Mater.* **198/199** 396
[59] Leng Q, Cros V, Schafer R, Fuss A, Grünberg P and Zinn W 1993 *J. Magn. Magn. Mater.* **126** 367
[60] Stiles M D 1999 *J. Magn. Magn. Mater.* **200** 322
[61] Bruno P 1999 *J. Phys.: Condens. Matter* **11** 9403
[62] Mathon J, Umerski A, Villeret M and Muniz R B 1999 *Phys. Rev.* B **59** 6344
[63] Ortega J E and Himpsel F J 1992 *Phys. Rev. Lett.* **69** 844
[64] Niklasson A M N, Mirbt S, Skriver H L and Johansson B 1996 *Phys. Rev.* B **53** 8509
[65] Drew A *et al* 2003 *PSI Scientific Report* Vol III, Paul Scherrer Institute, unpublished
[66] Kiefl R, MacFarlane W A, Morris G D, Amaudruz P, Arseneau D, Azumi H, Baartman R, Beals T R, Behr J and Bommas C 2003 *Physica* B **326** 189